ACS APPLIED MATERIALS & INTERFACES

Research Article

Cite This: ACS Appl. Mater. Interfaces 2017, 9, 36130-36136

www.acsami.org

Infrared Black Phosphorus Phototransistor with Tunable Responsivity and Low Noise Equivalent Power

Li Huang,[†,‡] Wee Chong Tan,[†,‡] Lin Wang,[†,‡] Bowei Dong,[†] Chengkuo Lee,[†] and Kah-Wee Ang*[,†,‡]

[†]Department of Electrical and Computer Engineering, National University of Singapore, 4 Engineering Drive 3, 117583, Singapore

[‡]Centre for Advanced 2D Materials, National University of Singapore, 6 Science Drive 2, 117546, Singapore

Supporting Information

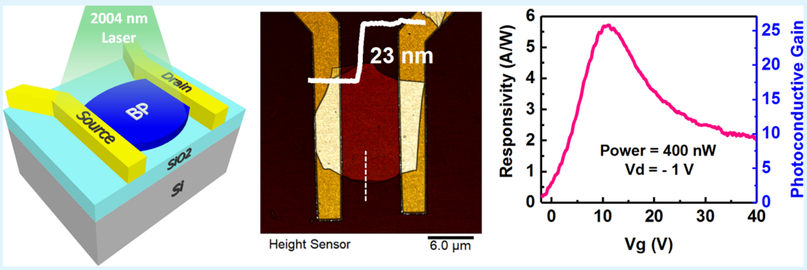

ABSTRACT: The narrow band gap property of black phosphorus (BP) that bridges the energy gap between graphene and transition metal dichalcogenides holds great promise for enabling broadband optical detection from ultraviolet to infrared wavelengths. Despite its rich potential as an intriguing building block for optoelectronic applications, however, very little progress has been made in realizing BP-based infrared photodetectors. Here, we demonstrate a high sensitivity BP phototransistor that operates at a short-wavelength infrared (SWIR) of 2 μm under room temperature. Excellent tunability of responsivity and photoconductive gain are acquired by utilizing the electrostatic gating effect, which controls the dominant photocurrent generation mechanism via adjusting the band alignment in the phototransistor. Under a nanowatt-level illumination, a peak responsivity of 8.5 A/W and a low noise equivalent power (NEP) of less than 1 pW/Hz$^{1/2}$ are achieved at a small operating source−drain bias of −1 V. Our phototransistor demonstrates a simple and effective approach to continuously tune the detection capability of BP photodetectors, paving the way to exploit BP to numerous low-light-level detection applications such as biomolecular sensing, meteorological data collection, and thermal imaging.

KEYWORDS: *short-wavelength infrared, black phosphorus, phototransistor, photodetector, electrostatic gating*

INTRODUCTION

Short-wavelength infrared (SWIR, 1−3 μm) photodetectors play a crucial role in the development of diversified applications such as cancer detection,[1] meteorological analysis,[2] optical telecommunication, and thermal imaging for night vision.[3] Among the commercially available SWIR photodetectors, the most common solution is InGaAs detectors with a typical responsivity of ~1.3 A/W.[4] Despite the decent performance and mature fabrication technology of InGaAs detectors, the lattice mismatch makes it difficult to integrate InGaAs with silicon-based integrated circuits.[5] Nonetheless, black phosphorus (BP), a two-dimensional material with a layered lattice structure, naturally eliminates the problem of lattice mismatch and is compatible with both silicon and flexible substrates.[6,7] Furthermore, a direct band gap of BP of 0.3 eV (when its thickness is larger than 4 nm)[8] enables broadband detection from ultraviolet to mid-infrared, making it possible to build BP-based photodetection systems with higher compactness and better sensitivity compared to its III−V compound counterparts.

Following the early works of BP photodetectors,[9−16] more investigations on near-to-mid-infrared photodetection based on BP have been reported recently.[17−27] The first reported thin-film BP photodetector achieved a responsivity of ~4.8 mA/W in the visible to 940 nm near-infrared spectrum.[10] Recently, a SWIR BP photodetector at 1550 nm has been demonstrated with a responsivity of 5 mA/W.[11] To improve the responsivity, silicon waveguide and metallic nanoplasmonics were integrated with BP, with an external responsivity of 0.214 A/W being achieved for the 1550 nm wavelength.[23] A recent work of a polarization-sensitive BP photodetector at 3.39 μm has extended detection spectrum of BP to mid-infrared.[18] A subsequent study on the time-resolved response of BP reveals the fast response of the materials in the mid-infrared with the rise/fall time on the order of pico-/nanoseconds.[21] In addition, successful integration of BP with silicon photonic crystals[19] has been reported for the 620−760 nm visible wavelengths. These investigations disclose the great potential of BP for infrared photodetection and have proven its compatibility with complex photonic structures. However, little attention has been devoted

Received: July 7, 2017
Accepted: September 29, 2017
Published: September 29, 2017

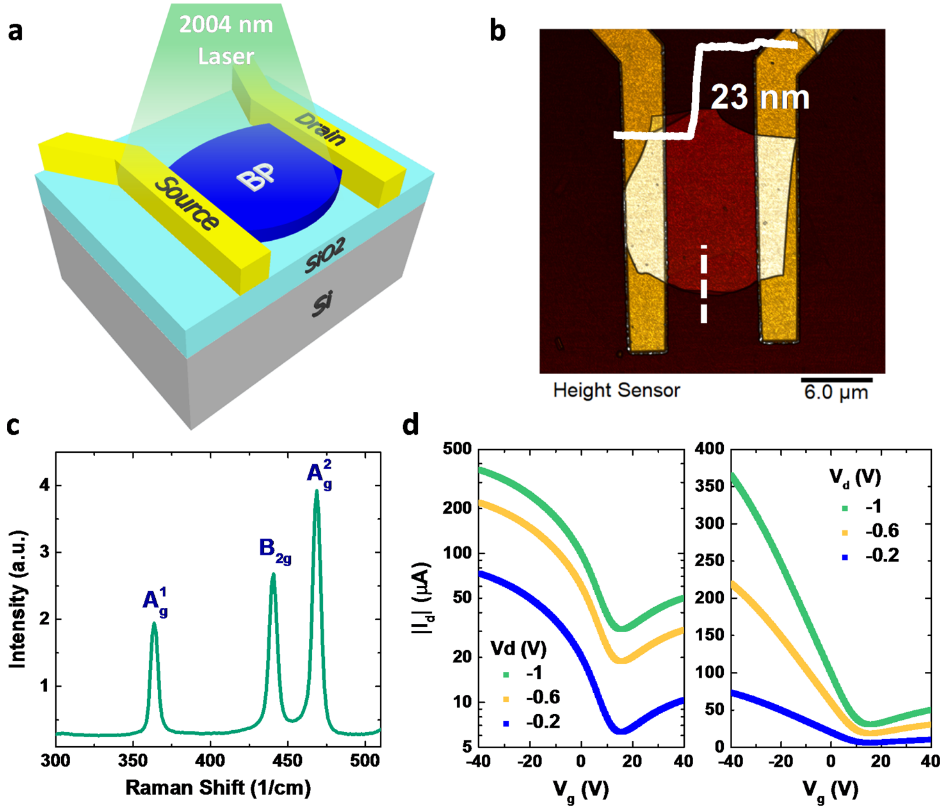

Figure 1. BP phototransistor structure and material characterizations. (a) Three-dimensional schematics. The laser is vertically illuminated from the top. (b) AFM image and height profile (white solid line) along the dashed line, showing a uniform BP flake with a thickness of ~23 nm. (c) Raman spectrum of the BP flake. The three peaks of the out-of-plane (A_g^1) and in-plane (B_{2g} and A_g^2) phonon modes are clearly presented. (d) Transfer characteristic of the BP phototransistor under varied source−drain biases in log and linear scales. The source−drain current is linearly proportional to the source−drain bias. The BP thickness of 23 nm maintains the gate control for tuning the phototransistor response. Hole conduction side shows a lower resistance than the electron conduction side. Minimum conductance point occurs at V_g = 15 V, where the carrier concentration is the lowest.

to BP photodetectors at 2 μm wavelength, a SWIR wavelength where unique applications exist. For example, some protein, lipids, and DNA molecules exhibit a characteristic reflectance peak at around 2 μm wavelength, which present useful fingerprint for cancer diagnostic.[1] Moreover, a detailed investigation of the ability to tune the photoresponse in a BP phototransistor by the electrostatic gating effect has not been reported at 2 μm.

In this work, we demonstrate a back-gate BP phototransistor with high sensitivity at 2 μm wavelength. The photocurrent generation mechanisms are investigated under different electrostatic gating effects, where a tunable responsivity with a peak value of 8.5 A/W is achieved. The tunable detection capability can be utilized to adapt the phototransistor to varying detecting conditions and requirements. In addition, the source−drain bias dependence of the noise equivalent power (NEP) and detectivity is analyzed and discussed. We show that the performance of the phototransistor can be optimized by tuning the gate and source−drain bias, and a NEP less than 1 pW/$Hz^{1/2}$ is obtained. High sensitivity is crucial for sensing applications such as biomedical detection where the signal to be identified might be extremely weak. On the basis of a simple device configuration, our phototransistor achieved the highest external responsivity and the lowest NEP among the reported SWIR BP photodetectors, without the assistance from hybrid systems such as waveguide or plasmonic structures, which makes BP a promising candidate for low-light-level SWIR detection.

EXPERIMENTAL METHODS

The BP thin flake was mechanically exfoliated from bulk BP crystals and transferred to a 90 nm SiO_2/n+Si substrate. The metal contacts were patterned by electron beam lithography (EBL), followed by the deposition of 3 nm Ni and 50 nm Au through magnetron sputtering. After lift-off to form the electrodes, a 20 nm Al_2O_3 passivation layer was grown by atomic layer deposition (ALD) at 200 °C, covering the BP channel to protect it from ambient degradation.[28] The phototransistor structure and BP flake characterization are shown in Figure 1. The atomic force microscopy (AFM) profile shows a uniform BP flake with a thickness of 23 nm (Figure 1b). At such a thickness, the flake possesses a small band gap close to the bulk, ensuring the occurrence of photon absorption at 2 μm, whereas the active channel maintains the gate control (Figure 1d) to tune the performance of the phototransistor.

RESULTS AND DISCUSSION

For a start, we measured the transfer curve of the phototransistor under different illumination powers. The photocurrent I_{ph} is extracted by the equation $I_{ph} = |I_{d,light}| - |I_{d,dark}|$, where $I_{d,light}$ and $I_{d,dark}$ are the source−drain current under illumination and in dark condition, respectively. In Figure 2a, the photocurrent, transconductance, and carrier concentration as a function of gate bias V_g are presented. The photoresponse dependence of the electrostatic gating effect is divided into three distinct regions, as marked in the middle part of Figure 2a. Negative photocurrents are observed in region I, which indicates a reduced transistor on-current under illumination. Notably, the photocurrent is shown to peak in region II at V_g =

DOI: 10.1021/acsami.7b09713
ACS Appl. Mater. Interfaces 2017, 9, 36130−36136

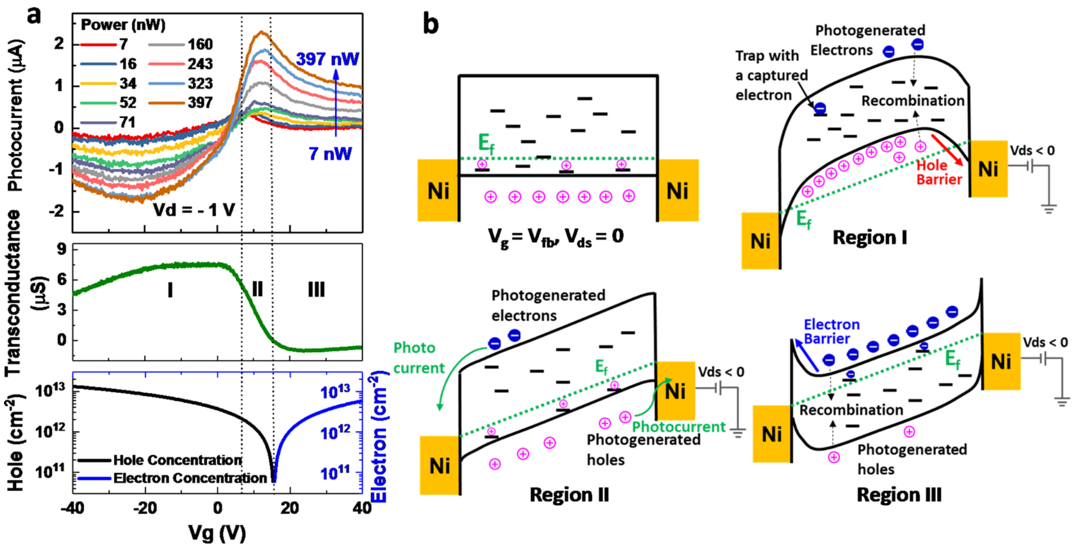

Figure 2. Photoresponse tuned by the electrostatic gating effect. (a) Top: dependence of the photocurrent on the gate bias under varied excitation powers. Middle: gate-dependent transconductance of the BP transistor. Bottom: gate-dependent carrier concentration in the BP channel. Three regions (I, II, and III) are divided according to the behavior of the photocurrent. In the heavily p-doped region (region I), the photocurrent is negative. The peak positive responsivity is achieved when the BP channel is lightly p-doped (region II). The photocurrent starts to drop monotonically when V_g moves into the n-doped region (region III); (b) band alignment of the BP channel and Ni contacts for different regions of the transfer curve, accounting for the distinct photoresponse characteristics in the three regions. E_F stands for the Fermi level. Region I: high carrier concentration and hole barrier because of band bending and large transconductance lead to negative photocurrent dominated by photogating effects. Region II: photoconductive effect is dominant as a result of reduced carrier concentration, transconductance, and lowered hole barrier, giving rise to a positive peak current. Region III: more positive gate voltage increases electron concentration and electron barrier. Therefore, a reduced photocurrent is observed.

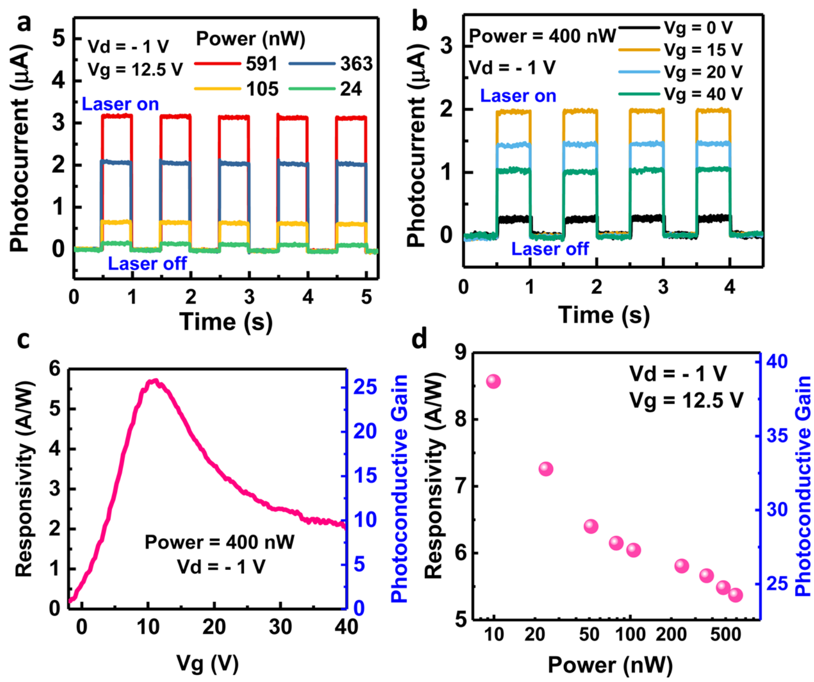

Figure 3. Performance of the BP phototransistor at a fixed source−drain bias (V_d) of −1 V. Temporal photoresponse for (a) different illumination powers on the device and (b) different gate biases. Responsivity and photoconductive gain under varied (c) gate biases and (d) illumination power. The phototransistor can be operated stably under nanowatt illumination power with the gate bias effectively tuning the photoresponse. Higher responsivity is achieved at a lower excitation power.

12.5 V when a lightly p-doped channel is induced near the off-state. However, when the V_g increases further into region III, photocurrent is observed to decrease monotonically. We show that the photocurrent of our device is predominantly contributed by two effects. The first one is the photoconductive effect where conductivity is increased by the photogenerated carriers. The photogenerated electron−hole pairs are then separated by the source−drain bias, thus giving rise to an elevated current. When the carrier concentration is low, there are less carrier scattering and recombination, so photocarriers

DOI: 10.1021/acsami.7b09713
ACS Appl. Mater. Interfaces 2017, 9, 36130−36136

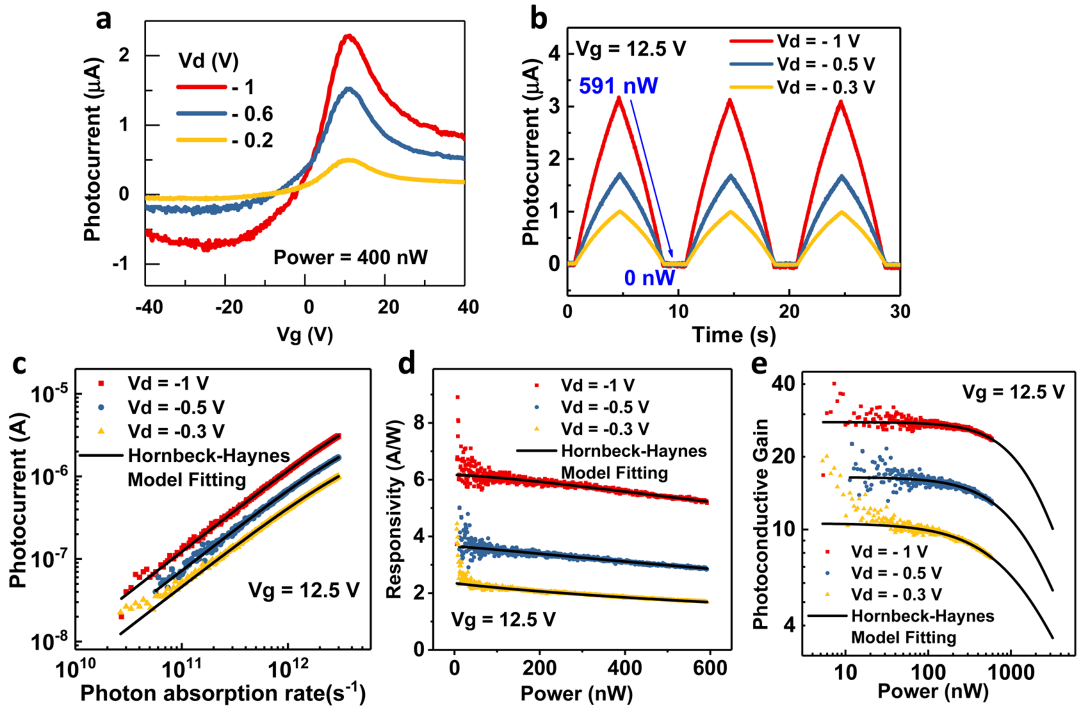

Figure 4. Photoresponse under different source−drain biases and illumination power. (a) Photocurrent is linearly proportional to the source−drain bias as a result of linearly increased lateral electric field in the channel as the source−drain bias increases. (b) Time response of the phototransistor as the laser output power is modulated by a triangle wave. (c) Photocurrent as a function of the photon absorption rate. (d) Responsivity and (e) photoconductive gain as a function of the illumination power, which are extracted from (b). Colored discrete data points: measured results. Black solid line: Hornbeck−Haynes model fitting.

can be efficiently collected by the electrodes. As a result, the photoconductive effect is most obvious at a low carrier concentration. The second contributor lies with the photogating effect[29] where traps in the forbidden band of BP capture electrons or holes and shift the threshold voltage of the transistor. The photocurrent caused by the threshold voltage shift ΔV_{th} can be expressed as $I_{ph} = g_m \cdot \Delta V_{th}$, where $g_m = \frac{dI_d}{dV_g}$ is the transconductance of the transistor. Depending on the region of transistor operation and the distribution of trap states, the photocurrent originating from this effect can be either positive or negative and is most prominent when the transconductance reaches its maximum value.

To explain the mechanisms in these regions, the energy band diagram of the BP channel and metal contacts is shown in Figure 2b. In region I, when a large negative gate bias is applied, the channel is heavily p-doped with the valence band bending downward at the BP/drain interface, leading to a barrier for holes moving from the channel to the drain contact. As a result, the photogenerated carriers suffer from severe scattering and recombination because of high carrier concentration and hole barrier height, with the photoconductive effect being repressed. Meanwhile, the empty electron traps in the forbidden band capture the photogenerated electrons and become negatively charged, resulting in a threshold shift to a more negative value. The large transconductance in region I, in conjunction with the negative threshold shift, gives rise to a dominating negative photocurrent which overwhelms the weak photoconductive effect. As the gate bias is increased in region II, a reduced transconductance is observed wherein the threshold shift plays a weaker role in contributing to the total photocurrent. At the same time, band bending at the BP/drain interface decreases, and the carrier concentration is considerably reduced by the gate voltage, which enables photogenerated electron−hole pairs to be efficiently collected by the electrodes before recombination. Therefore, in region II, the photoconductive effect is dominant and we attribute the positive photocurrent peak to the highly efficient photocarrier collection. When a larger positive gate bias is applied, transconductance remains small, so the photogating effect is negligible and the photoconductive effect is still dominating. Meanwhile, negatively charged electrons are induced in the channel and the conduction band bends upward at the BP/source interface, acting as an electron barrier which increases the probability of carrier recombination. This leads to a lowered photocurrent in region III. The behavior of gate dependence in the three regions indicates the gate tunability functions through controlling the carrier concentration in the BP channel, modifying the transconductance of the transistor and adjusting the electron−hole barrier height. Although there are other methods such as chemical doping[30] to tune the sensitivity of BP transistors, the electrostatic gating method in this work is a more straightforward and effective approach and has the advantage of being nondestructive and reversible. Figure 3a,b shows that the device is capable of operating stably as the laser is switched on and off under various illumination powers of nanowatt levels and different gate biases, respectively.

As an initial step to evaluate the performance of the phototransistor, we analyze the responsivity and photoconductive gain under a fixed source−drain bias (V_d) of −1 V. The responsivity is defined by $R = I_{ph}/P$, where P is the power illuminated on the BP channel region. Photoconductive gain indicates how many carriers contributing to the photocurrent can be generated by one absorbed photon, and it is calculated by the equation $G = (I_{ph}/P_{abs})(h\nu/q)$, where P_{abs} is

DOI: 10.1021/acsami.7b09713
ACS Appl. Mater. Interfaces 2017, 9, 36130−36136

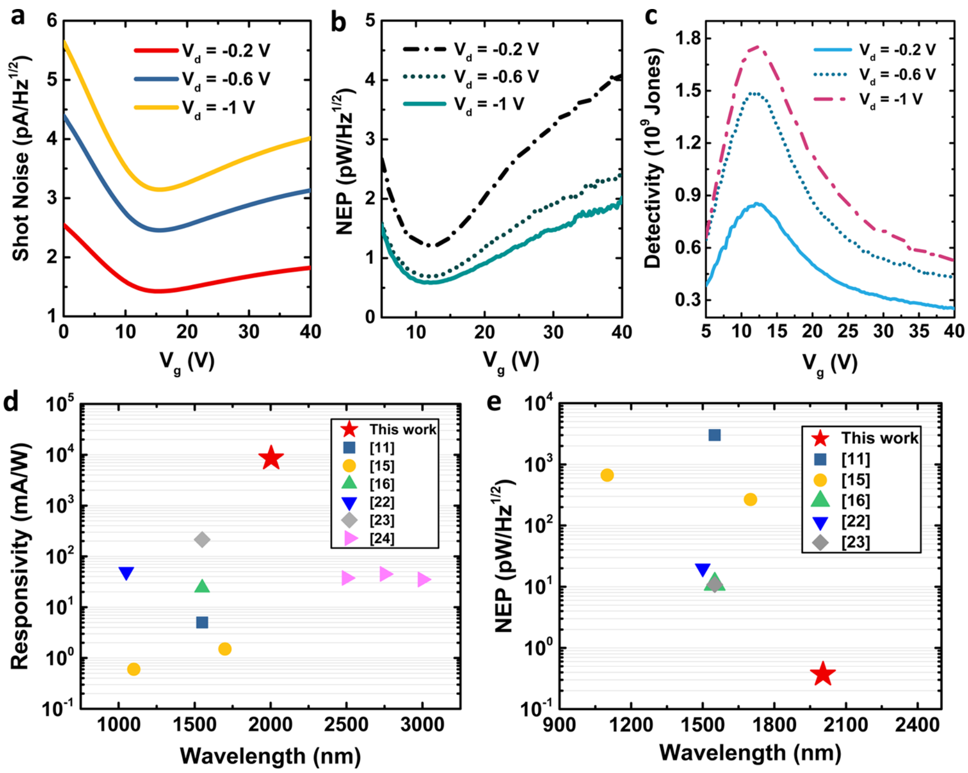

Figure 5. Noise and detection limit of the phototransistor. (a) Shot noise calculated from the dark current. (b) NEP tuned by the gate voltage, indicating the detection limit of our phototransistor. With higher source−drain bias (V_d), the shot noise increases slower than the photocurrent; thus, lower NEP is observed for larger V_d. A minimum NEP less than 1 pW/Hz$^{1/2}$ was achieved at $V_g \approx 12.5$ V, where the noise level is near the lowest point and the photocurrent is optimized. (c) Detectivity at various operation conditions. A peak detectivity on the order of 10^9 jones was achieved. Benchmark of reported SWIR (1−3 μm) BP photodetectors in terms of responsivity (d) and NEP (e).

the power absorbed by the channel, h is Planck's constant, ν is the frequency of the excitation light, and q is the elementary charge. The absorbed power $P_{abs} = \eta P$, where η is the absorption percentage and is assumed to be 13.7% at 2 μm wavelength for 23 nm BP (Supporting Information IV). Figure 3c shows the responsivity and photoconductive gain being continuously tuned by the gate bias. An increased responsivity was observed with reduced excitation power (Figure 3d), possibly because of less frequent carrier recombination and longer carrier lifetime at weaker illumination. At around 10 nW illumination power, a peak responsivity of 8.5 A/W and a photoconductive gain of 10.5 were achieved. The responsivity of our device is a few times higher than the commercially available InGaAs detectors.

Apart from the electrostatic gating effect, we next investigate the source−drain bias dependence, another factor which determines the performance of the device. Under different source−drain biases, the photocurrent is shown in Figure 4a, which confirms that the gate control of the photoresponse remains effective for all the source−drain biases being studied. Figure 4b presents the time-resolved photoresponse under different source−drain biases when the output power of the laser is modulated by a triangle wave, from which the illumination power dependence of the photocurrent, responsivity, and photoconductive gain for varied source−drain biases is extracted and displayed in Figure 4c−e, respectively. The Hornbeck−Haynes model is adopted to fit the measured data.[31] According to this model, the relationship between the photoresponse and illumination power is described as

$$I_{ph} = q\eta\frac{\tau_0}{\tau_{tr}}\cdot\frac{F}{1+\left(\frac{F}{F_0}\right)^n} \quad (1)$$

$$G = \frac{I_{ph}}{qF} = \eta\frac{\tau_0}{\tau_{tr}}\cdot\frac{1}{1+\left(\frac{F}{F_0}\right)^n} \quad (2)$$

where τ_0 and $\tau_{tr} = \frac{L^2}{\mu_h V_d}$ (L is the channel length, V_d is the source−drain bias, and μ_h is the hole mobility, which can be obtained from the transfer curve) are the carrier lifetime and transit time; $F = \frac{\eta P}{h\nu}$ is the photon absorption rate; F_0 is the photon absorption rate when trap saturation occurs; and n is a fitting parameter. As illustrated in eq 2, a larger source−drain bias would induce a stronger lateral electric field in the channel, leading to an enhanced photoconductive gain. The fitting curves are represented in black solid line in Figure 4c−e. From the fitting results, a carrier lifetime τ_0 of ∼1.02 μs is derived (Supporting Information IV). As a result, the 3 dB bandwidth $f_{3dB} = \frac{1}{2\pi\tau_0}$ is calculated to be ∼0.156 MHz, indicating that the device has the potential for high-speed operation.

To evaluate the detection limit of our device, we then analyze the current noise, NEP, and detectivity of this phototransistor. The noise of this phototransistor mainly consists of three parts: $1/f$ noise, shot noise, and Johnson noise. The $1/f$ noise mainly originates from the defects in the channel acting as traps[32] and could be a dominating element in the total noise at low frequencies. Shot noise is determined by the dark current according to the equation

DOI: 10.1021/acsami.7b09713
ACS Appl. Mater. Interfaces 2017, 9, 36130−36136

$$\text{Shot noise} = \sqrt{2qI_{\text{dark}}\Delta f} \quad (3)$$

where Δf is the bandwidth. The shot noise of our phototransistor is shown in Figure 5, and it is in the same level as the previously reported mid-infrared BP photodetector.[18] Depending on the operating frequency and gate bias, the $1/f$ noise can be either larger, comparable, or smaller than the shot noise. Johnson noise is caused by the thermal agitation of charge carriers in the channel and is expressed as $\sqrt{\frac{4k_BT\Delta f}{R}}$, where R is the channel resistance and k_B is the Boltzmann constant. At room temperature, the Johnson noise of our device is negligible because it is much smaller than the shot noise when $V_d = -1$ V (Supporting Information V, Figure S4). Near the off-state of the transistor when the dark current is largely reduced by the applied gate bias, the value of the total noise gets closer to the shot noise.[18] Moreover, the $1/f$ noise decays as the operating frequency increases. Hence, the shot noise is the lower limit for the total noise of our phototransistor. In the following calculations, we approximate the total noise with the shot noise calculated from the measured dark current. The NEP is defined as the excitation power needed to generate a signal equal to the noise level in one hertz bandwidth; therefore, it characterizes the detection limit of a detector.[33] Detectivity is the sensitivity normalized with the active area of a photodetector; thus, it can be used to compare the performance of different photodetectors with varied sizes. The NEP and detectivity are estimated and shown in Figure 5 according to the following expressions.

$$\text{NEP} = \frac{\text{noise}}{\text{responsivity}} \quad (4)$$

$$\text{Detectivity} = \frac{\sqrt{A}}{\text{NEP}} \quad (5)$$

where A is the device active area. Calculation shows that the NEP of our device is on the order of picowatt per square root of hertz, which is at least 1 order of magnitude lower than the reported SWIR BP photodetectors.[11,15,16,22,23] The gate dependence of detectivity exhibits the same trend as that of the photocurrent and responsivity, with a peak value at $V_g = 12.5$ V, where responsivity is optimized and shot noise is near its minimum point. With increasing source−drain bias, the photocurrent shows a faster increment than the shot noise. When V_d is changed from −0.6 to −1 V, the photocurrent increases by 52%, whereas only 28% increment is incurred in the shot noise. Consequently, the detectivity is enhanced when larger V_d is applied, suggesting that the source−drain bias can be exploited as another degree of tunability for further improvement of the performance of the device. At the optimal operation condition, when $V_g = 12.5$ V and $V_d = -1$ V, a NEP of less than 1 pW/Hz$^{1/2}$ is achieved, implying that our device has the potential to detect subpicowatt illumination power with half a second integration time.

CONCLUSIONS

In conclusion, a high sensitivity BP phototransistor has been demonstrated at a SWIR of 2 μm. The responsivity and NEP of the phototransistor can be effectively modulated through the electrostatic gating effect, which enables an instant and dynamic control of the detecting capability to meet various photodetection requirements. This BP phototransistor outperformed its III−V compound counterparts in terms of responsivity and is capable of being further improved by readily achievable methods such as reducing the channel length or adopting interdigitated electrodes. Additionally, the NEP in the range of picowatt per square root of hertz endows our BP phototransistor with a potential for weak signal detection applications such as biomedical sensing. The high responsivity and low NEP, together with good compatibility of BP with silicon substrates, make it a potential alternative to the traditional SWIR photodetectors and predict a promising future for the high-performance integration of BP and Si photonics in the infrared wavelengths.

METHODS

Device Fabrication and Characterization. The device was fabricated on a heavily n-doped Si substrate covered with 90 nm SiO_2. After exfoliation and transfer of BP onto the substrate, the sample was spin-coated with poly(methyl methacrylate) (950k A5) and baked for 2 min at 180 °C. Then, EBL (Nova NanoSEM 230) was used to pattern the electrodes. Following the development of the e-beam resist [developer: isopropyl alcohol/methyl isobutyl ketone (1:3)], 3 nm Ni and 50 nm Au were deposited by magnetron sputtering to form the metal contacts. Subsequent to the lift-off process in acetone, a 20 nm Al_2O_3 layer was grown by ALD at 200 °C, covering the BP channel as passivation. After the fabrication process is completed, AFM (Bruker) was measured in a tapping mode to obtain the height profile of the device. Raman spectroscopy was measured using a WITec Alpha 300R instrument with the 532 nm laser.

Electrical and Photocurrent Measurement. Source−drain bias and gate voltage were applied to the phototransistor through a probe station (Micromanipulator). The source electrode was connected to the ground, and the back-gate bias was applied on the heavily doped Si substrate. A parameter analyzer (Agilent 4155B) was used to control the biases and measure the source−drain current. The laser source is a continuous wave laser diode with a 2004 nm output wavelength (Eblana Photonics DX-01206 EP2004-0-DM-DX1-FM). The laser output was guided to the top of the sample surface with a single-mode fiber (Thorlabs SM2000). Illumination power on device is normalized by the equation $P = P_0 \cdot \frac{\text{device area}}{\text{laser spot size}}$, where P_0 is the laser output power. The temporal response of the device was acquired by fixing the source−drain and gate bias and modulating the laser diode with a function generator.

ASSOCIATED CONTENT

Supporting Information

The Supporting Information is available free of charge on the ACS Publications website at DOI: 10.1021/acsami.7b09713.

Device and optical characterizations, additional experimental details, and Hornbeck−Haynes model fitting results of the photoresponse (PDF)

AUTHOR INFORMATION

Corresponding Author

*E-mail: eleakw@nus.edu.sg.

ORCID

Li Huang: 0000-0002-2188-3178

Chengkuo Lee: 0000-0002-8886-3649

Kah-Wee Ang: 0000-0003-1919-3351

Author Contributions

K.-W.A. supervised the project. L.H. carried out the experiments and characterization. All authors analyzed the data, discussed the results, and contributed to the final manuscript.

Notes

The authors declare no competing financial interest.

DOI: 10.1021/acsami.7b09713
ACS Appl. Mater. Interfaces 2017, 9, 36130−36136

■ ACKNOWLEDGMENTS

This research is supported by the National University of Singapore Faculty Research Committee Grants (R-263-000-B21-133 and R-263-000-B21-731), A*STAR Science and Engineering Research Council Grant (no. 152-70-00013), National Research Foundation Competitive Research Programs (NRF-CRP15-2015-01 and NRF-CRP15-2015-02), and by the National Research Foundation, Prime Minister's Office, Singapore under its medium-sized centre program.

■ REFERENCES

(1) Hirosawa, N.; Sakamoto, Y.; Katayama, H.; Tonooka, S.; Yano, K. In Vivo Investigation of Progressive Alterations in Rat Mammary Gland Tumors by Near-Infrared Spectroscopy. *Anal. Biochem.* **2002**, *305*, 156−165.

(2) Soderblom, L. A.; Britt, D. T.; Brown, R. H.; Buratti, B. J.; Kirk, R. L.; Owen, T. C.; Yelle, R. V. Short-Wavelength Infrared (1.3−2.6 μm) Observations of the Nucleus of Comet 19P/Borrelly. *Icarus* **2004**, *167*, 100−112.

(3) Hansen, M. P.; Malchow, D. S. Overview of SWIR Detectors, Cameras, and Applications. *Proc. SPIE* **2008**, *6939*, 69390I.

(4) http://www.hamamatsu.com/resources/pdf/ssd/ingaas_kird0005e.pdf 2017.

(5) Razeghi, M.; Nguyen, B.-M. Advances in Mid-Infrared Detection and Imaging: A Key Issues Review. *Rep. Prog. Phys.* **2014**, *77*, 082401.

(6) Xia, F.; Wang, H.; Xiao, D.; Dubey, M.; Ramasubramaniam, A. Two-dimensional Material Nanophotonics. *Nat. Photonics* **2014**, *8*, 899−907.

(7) (a) Zhu, W.; Yogeesh, M. N.; Yang, S.; Aldave, S. H.; Kim, J.-S.; Sonde, S.; Tao, L.; Lu, N.; Akinwande, D. Flexible Black Phosphorus Ambipolar Transistors, Circuits and AM Demodulator. *Nano Lett.* **2015**, *15*, 1883−1890. (b) Liu, Y.; Ang, K.-W. Monolithically Integrated Flexible Black Phosphorus Complementary Inverter Circuits. *ACS Nano* **2017**, *11*, 7416−7423.

(8) Ling, X.; Wang, H.; Huang, S.; Xia, F.; Dresselhaus, M. S. The Renaissance of Black Phosphorus. *Proc. Natl. Acad. Sci. U.S.A.* **2015**, *112*, 4523−4530.

(9) Xia, F.; Wang, H.; Jia, Y. Rediscovering Black Phosphorus as an Anisotropic Layered Material for Optoelectronics and Electronics. *Nat. Commun.* **2014**, *5*, 4458.

(10) Buscema, M.; Groenendijk, D. J.; Blanter, S. I.; Steele, G. A.; van der Zant, H. S. J.; Castellanos-Gomez, A. Fast and Broadband Photoresponse of Few-Layer Black Phosphorus Field-Effect Transistors. *Nano Lett.* **2014**, *14*, 3347−3352.

(11) Engel, M.; Steiner, M.; Avouris, P. Black Phosphorus Photodetector for Multispectral, High-Resolution Imaging. *Nano Lett.* **2014**, *14*, 6414−6417.

(12) Buscema, M.; Groenendijk, D. J.; Steele, G. A.; van der Zant, H. S. J.; Castellanos-Gomez, A. Photovoltaic Effect in Few-Layer Black Phosphorus PN Junctions Defined by Local Electrostatic Gating. *Nat. Commun.* **2014**, *5*, 4651.

(13) Deng, Y.; Luo, Z.; Conrad, N. J.; Liu, H.; Gong, Y.; Najmaei, S.; Ajayan, P. M.; Lou, J.; Xu, X.; Ye, P. D. Black Phosphorus−Monolayer MoS_2 Van der Waals Heterojunction P−N Diode. *ACS Nano* **2014**, *8*, 8292−8299.

(14) Wu, J.; Koon, G. K. W.; Xiang, D.; Han, C.; Toh, C. T.; Kulkarni, E. S.; Verzhbitskiy, I.; Carvalho, A.; Rodin, A. S.; Koenig, S. P.; Eda, G.; Chen, W.; Neto, A. H. C.; Özyilmaz, B. Colossal Ultraviolet Photoresponsivity of Few-Layer Black Phosphorus. *ACS Nano* **2015**, *9*, 8070−8077.

(15) Yuan, H.; Liu, X.; Afshinmanesh, F.; Li, W.; Xu, G.; Sun, J.; Lian, B.; Curto, A. G.; Ye, G.; Hikita, Y.; Shen, Z.; Zhang, S.-C.; Chen, X.; Brongersma, M.; Hwang, H. Y.; Cui, Y. Polarization-Sensitive Broadband Photodetector Using a Black Phosphorus Vertical P−N Junction. *Nat. Nanotechnol.* **2015**, *10*, 707−713.

(16) Youngblood, N.; Chen, C.; Koester, S. J.; Li, M. Waveguide-Integrated Black Phosphorus Photodetector with High Responsivity and Low Dark Current. *Nat. Photonics* **2015**, *9*, 247−252.

(17) Huang, M.; Wang, M.; Chen, C.; Ma, Z.; Li, X.; Han, J.; Wu, Y. Broadband Black-Phosphorus Photodetectors with High Responsivity. *Adv. Mater.* **2016**, *28*, 3481−3485.

(18) Guo, Q.; Pospischil, A.; Bhuiyan, M.; Jiang, H.; Tian, H.; Farmer, D.; Deng, B.; Li, C.; Han, S.-J.; Wang, H.; Xia, Q.; Ma, T.-P.; Mueller, T.; Xia, F. Black Phosphorus Mid-Infrared Photodetectors with High Gain. *Nano Lett.* **2016**, *16*, 4648−4655.

(19) Wang, T.; Hu, S.; Chamlagain, B.; Hong, T.; Zhou, Z.; Weiss, S. M.; Xu, Y.-Q. Visualizing Light Scattering in Silicon Waveguides with Black Phosphorus Photodetectors. *Adv. Mater.* **2016**, *28*, 7162−7166.

(20) Zhang, G.; Huang, S.; Chaves, A.; Song, C.; Özçelik, V. O.; Low, T.; Yan, H. Infrared Fingerprints of Few-Layer Black Phosphorus. *Nat. Commun.* **2017**, *8*, 14071.

(21) Suess, R. J.; Leong, E.; Garrett, J. L.; Zhou, T.; Salem, R.; Munday, J. N.; Murphy, T. E.; Mittendorff, M. Mid-Infrared Time-Resolved Photoconduction in Black Phosphorus. *2D Mater.* **2016**, *3*, 041006.

(22) Wang, L.; Liu, C.; Chen, X.; Zhou, J.; Hu, W.; Wang, X.; Li, J.; Tang, W.; Yu, A.; Wang, S.-W.; Lu, W. Toward Sensitive Room-Temperature Broadband Detection from Infrared to Terahertz with Antenna-Integrated Black Phosphorus Photoconductor. *Adv. Funct. Mater.* **2017**, *27*, 1604414.

(23) Chen, C.; Youngblood, N.; Peng, R.; Yoo, D.; Mohr, D. A.; Johnson, T. W.; Oh, S.-H.; Li, M. Three-Dimensional Integration of Black Phosphorus Photodetector with Silicon Photonics and Nanoplasmonics. *Nano Lett.* **2017**, *17*, 985−991.

(24) Xu, M.; Gu, Y.; Peng, R.; Youngblood, N.; Li, M. Black Phosphorus Mid-Infrared Photodetectors. *Appl. Phys. B: Lasers Opt.* **2017**, *123*, 130.

(25) Na, J.; Park, K.; Kim, J. T.; Choi, W. K.; Song, Y.-W. Air-Stable Few-Layer Black Phosphorus Phototransistor for Near-Infrared Detection. *Nanotechnology* **2017**, *28*, 085201.

(26) Ye, L.; Wang, P.; Luo, W.; Gong, F.; Liao, L.; Liu, T.; Tong, L.; Zang, J.; Xu, J.; Hu, W. Highly Polarization Sensitive Infrared Photodetector Based on Black Phosphorus-on-WSe_2 Photogate Vertical Heterostructure. *Nano Energy* **2017**, *37*, 53−60.

(27) (a) Ye, L.; Li, H.; Chen, Z.; Xu, J. Near-Infrared Photodetector Based on MoS_2/Black Phosphorus Heterojunction. *ACS Photonics* **2016**, *3*, 692−699. (b) Liu, Y.; Cai, Y.; Zhang, G.; Zhang, Y.-W.; Ang, K.-W. Al-Doped Black Phosphorus p-n Homojunction Diode for High Performance Photovoltaic. *Adv. Funct. Mater.* **2017**, *27*, 1604638.

(28) (a) Wood, J. D.; Wells, S. A.; Jariwala, D.; Chen, K.-S.; Cho, E.; Sangwan, V. K.; Liu, X.; Lauhon, L. J.; Marks, T. J.; Hersam, M. C. Effective Passivation of Exfoliated Black Phosphorus Transistors Against Ambient Degradation. *Nano Lett.* **2014**, *14*, 6964−6970. (b) Tan, W. C.; Cai, Y.; Ng, R. J.; Huang, L.; Feng, X.; Zhang, G.; Zhang, Y.-W.; Nijhuis, C. A.; Liu, X.; Ang, K.-W. Few-Layer Black Phosphorus Carbide Field-Effect Transistor via Carbon Doping. *Adv. Mater.* **2017**, *29*, 1700503.

(29) Buscema, M.; Island, J. O.; Groenendijk, D. J.; Blanter, S. I.; Steele, G. A.; van der Zant, H. S. J.; Castellanos-Gomez, A. Photocurrent Generation with Two-Dimensional Van der Waals Semiconductors. *Chem. Soc. Rev.* **2015**, *44*, 3691−3718.

(30) Xu, Y.; Yuan, J.; Fei, L.; Wang, X.; Bao, Q.; Wang, Y.; Zhang, K.; Zhang, Y. Selenium-Doped Black Phosphorus for High-Responsivity 2D Photodetectors. *Small* **2016**, *12*, 5000−5007.

(31) Soci, C.; Zhang, A.; Xiang, B.; Dayeh, S. A.; Aplin, D. P. R.; Park, J.; Bao, X. Y.; Lo, Y. H.; Wang, D. ZnO Nanowire UV Photodetectors with High Internal Gain. *Nano Lett.* **2007**, *7*, 1003−1009.

(32) Clément, N.; Nishiguchi, K.; Fujiwara, A.; Vuillaume, D. One-by-One Trap Activation in Silicon Nanowire Transistors. *Nat. Commun.* **2010**, *1*, 92.

(33) Richards, P. L. Bolometers for Infrared and Millimeter Waves. *J. Appl. Phys.* **1994**, *76*, 1−24.